

Novel strategy to model deformation-induced strand contraction/dilatation during mechanical reduction

Rui Guan^{a,c,d}, Christian M.G. Rodrigues^{a,*}, Cheng Ji^c, Miaoyong Zhu^c, Shengli Li^d, Menghuai Wu^a, Abdellah Kharicha^{a,b}, Alexander Vakhrushev^b, Andreas Ludwig^a

^a Department Metallurgy, Montanuniversitaet Leoben, Franz-Josef Street 18, Leoben 8700, Austria

^b Christian-Doppler Laboratory for Metallurgical Application of Magnetohydrodynamics, Montanuniversitaet Leoben, Franz-Josef Street 18, Leoben 8700, Austria

^c School of Metallurgy, Northeastern University, 3-11, Wenhua Road, Shenyang 110816, China

^d School of Materials and Metallurgy, University of Science and Technology Liaoning, 189, Qianshanzhong Road, Anshan 114051, China

ARTICLE INFO

Article history:

Received 21 July 2022

Revised 11 October 2022

Accepted 14 October 2022

Available online 19 October 2022

Keywords:

Contraction/dilatation

Two-phase

Viscoplastic model

Solid deformation

Macrosegregation

ABSTRACT

When a strand is subjected to rolling and pressing during mechanical reduction (MR), deformation-induced strand contraction or dilatation can occur. A novel modeling strategy has been designed to account for this mechanism in a two-phase Eulerian–Eulerian volume-average model with a fixed geometry. The strategy is based on the following ideas: (1) during MR, the pressing force from the rolls to the solidifying strand leads to the compression of the viscoplastic network that causes melt to be squeezed out of that region; (2) if the pressing is strong enough to cause the melt to penetrate the surrounding solid shell, the strand deflects outwards (the dilatation state); (3) as the melt flow weakens and the following pair of rolls approaches, the “expanded” strand structure is forced to go back to its original form (the contraction state). Numerically, special Robin type boundary conditions have been imposed on the strand surface to comply with the above description while maintaining a fixed domain. Strand deflection has been estimated and correlates well with the mush deformation intensity and solidification evolution during the casting process. Macrosegregation is also discussed based on the strand deflection and deformation parameters.

© 2022 The Authors. Published by Elsevier Inc.
This is an open access article under the CC BY license
(<http://creativecommons.org/licenses/by/4.0/>)

1. Introduction

Macrosegregation is a common solidification defect that causes a degradation of the mechanical properties of castings [1]. Many researchers dedicated their careers to comprehend macrosegregation and found many causes for its formation. Some of the main causes that lead to macrosegregation formation are: thermal and solutal buoyancy-driven convection flow of the liquid melt [2], solidification-induced feeding flow [3], sedimentation of equiaxed grains [4], and mush deformation [5]. In most castings, all phenomena are present and play a critical role in the evolution of the cast.

* Corresponding author.

E-mail address: christian.gomes-rodrigues@unileoben.ac.at (C.M.G. Rodrigues).

Nomenclature

List of symbols

A, B	rheological parameters (-)
c	solute concentration [wt.%]
c_0	initial solute concentration [wt.%]
c^*	equilibrium species conc. [wt.%]
$C_{\ell s}$	species transfer rate [kg/m ³ /s]
c_p	heat capacity [J/K/kg]
D	diffusion coefficient [m ² /s]
g	volume fraction (-)
g_s^p	packing solid fraction (-)
h	enthalpy [J/kg]
$H_{\ell s}$	enthalpy transfer rate [J/m ³ /s]
h_c	heat transfer coefficient [W/m ² /K]
k	redistribution coefficient (-)
K_v	viscoplastic consistency (Pa·s)
m	strain-rate sensitivity (-)
$m_{\ell s}$	liquidus slope (-)
$M_{\ell s}$	mass transfer rate [kg/m ³ /s]
n	number density of grains [m ⁻³]
$N_{\text{cell}}^A, N_{\text{cell}}^B$	total number of cells on the surface of sub-domain A and B (-)
N_{celli}^B	cell number along the patch of sub-domain B (-)
p	pressure [N/m ²]
r	average radius of equiaxed crystal [m]
S_f^A	total patch area in sub-domain A (m ²)
$S_{\ell s}$	specific surface area of crystals [m ⁻¹]
t	time [s]
T	temperature [K]
T_{liq}	liquidus Temperature [K]
u^*	average velocity [m/s]
$U_{\ell s}$	momentum transfer rate [kg/m ² /s ²]
$U_{\ell s}^d$	source term for drag force [kg/m ² /s ²]
v	velocity [m/s]
v_r	interfacial growth vel. of crystal [m/s]
v_x^A, v_x^B	average velocity along the cast direction in sub-domain A and B [m/s]
v_y^B	velocity normal to the casting direction in sub-domain B [m/s]
$\dot{\epsilon}_s^{\text{eq}}$	equivalent strain rate [1/s]
φ_{imp}	impingement factor (-)
ϕ_f^A	volumetric flow rate [m ³ /s]
λ	thermal conductivity [W/m/K]
ρ	density [kg/m ³]
τ	viscous stress [N/m ²]

Sub/Superscripts

app	apparent
eff	effective
ℓ	liquid phase
mix	mixture rule
s	solid phase

Several solidification models have been developed to simulate solidification and macrosegregation. The earliest attempt was the mixture continuum model [2,6,7], which reduced the two-phase system to a one-phase model by considering each variable as mixture quantities (i.e., only one set of mixture conservation equation was used). Later, solidification models based on a Euler-Euler volume-average approach were proposed [8–10], where a set of conservation equations were solved for each phase in a coupled manner. This Euler-Euler method proved to be more adequate for simulating the macrosegregation from multiphase transport phenomena, as the relative motion between phases could be captured. This work has been further extended by research groups like Ludwig and Wu [3,4,11] and Combeau et al. [12] to include multiple physics

Table 1
Volume-average conservation equations.

Mass:	$\frac{\partial(\rho_i \rho_i)}{\partial t} + \nabla \cdot (\mathbf{g}_i \rho_i \mathbf{v}_i) = \mp M_{\ell s}$	(1)
Momentum:	$\frac{\partial(\mathbf{g}_i \rho_i \mathbf{v}_i)}{\partial t} + \nabla \cdot (\mathbf{g}_i \rho_i \mathbf{v}_i \mathbf{v}_i) = -\mathbf{g}_i \nabla p + \nabla \cdot (\mathbf{g}_i \boldsymbol{\tau}_i^{\text{eff}}) \mp U_{\ell s}$	(2)
Species:	$\frac{\partial(\mathbf{g}_i \rho_i c_i)}{\partial t} + \nabla \cdot (\mathbf{g}_i \rho_i \mathbf{v}_i c_i) = \nabla \cdot (\mathbf{g}_i \rho_i D_i \nabla c_i) \mp C_{\ell s}$	(3)
Enthalpy:	$\frac{\partial(\mathbf{g}_i \rho_i h_i)}{\partial t} + \nabla \cdot (\mathbf{g}_i \rho_i \mathbf{v}_i h_i) = \nabla \cdot (\frac{\lambda_i}{c_{p,i}} \nabla h_i) \mp H_{\ell s}$	(4)
Grain transport:	$\frac{\partial n}{\partial t} + \nabla \cdot (\mathbf{v}_s n) = 0$	(5)

occurring during casting. These advancements enabled both groups to simulate the typical macrosegregation patterns found in industrial casting processes.

Nevertheless, mush deformation is still a macrosegregation-inducing mechanism that is often neglected in general solidification models because of the complexity in its numerical implementation. Mush deformation leads to a compression or expansion of the dendritic network which can occur due to thermal constraints (e.g., in direct chill casting), metallostatic pressure (e.g., in continuous casting of steel), or mechanically applied strand thickness reduction (e.g., in twin-roll casting or during the “soft reduction” stage at the end of the solidification process in the continuous casting of steel). Viscoplastic constitutive laws for semi-solid alloys have been proposed by Nguyen et al. [13] based on isothermal uniaxial compression and drained die pressing experiments for the A356 alloy. According to the authors, pressing of the solid skeleton drives the liquid flow behavior, which in turn affects the stress in the solid phase. This viscoplastic behavior starts at a solid fraction of 0.57. Subsequent research has extended the characterization of the viscoplastic behavior of alloys [14], under different stress-strain conditions [15] and alloy properties [16].

Koshikawa et al. [17] investigated the macrosegregation formation mechanism due to solid deformation during punch pressing of solidifying steel ingots. A negative solid divergence was found in the ingot center, which was an indication of mush compression. Similarly, a negative macrosegregation was found in the ingot center as well. In continuous casting, owing to the large metallostatic pressure, the strand is subjected to successive contraction/dilatation states (also referred to as bulging), which causes the formation of a centerline macrosegregation. Most numerical models employed to simulate bulging-induced macrosegregation are still very incomplete because they generally are limited to a certain range of the solidification process, impose a pre-defined bulging profile to the strand, or do not consider the actual deformation behavior of the solid skeleton [18–20]. The main exception is the work of Fachinotti et al. [21] who proposed a complex model based on the finite-element method (FEM) that coupled mass, momentum, energy, and solute transfer equations with the viscoplastic behavior of materials. The model was applied to the steel slab continuous casting process, and the authors demonstrated the impact of the deformation of the solid skeleton on macrosegregation when the cast strand was subjected to consecutive effects of bulging. In twin-roll casting, Rodrigues et al. [22] also considered the viscoplastic behavior of the dendritic network and found that the relative motion between the solid and liquid phases caused by the deformation of the mush during pressing and rolling influenced the macrosegregation profiles observed in the final metal strip. A parameter study was performed to determine the optimal process window (considering roll speed, cooling conditions of the rolls, etc.) to achieve minimal composition variation in the final strip [23]. Recently a mixture formulation of the Norton-Hoff type viscoplastic model was applied by some of the authors to simulate the growth of the solidified shell in a thin slab continuous casting mold [24].

In the present paper, we extend our proposed viscoplastic model [22,23] to study the strand deflection (i.e. contraction/dilatation states) induced by the mush deformation during mechanical reduction (MR) of an octuplet-roll casting technique. This design comprises some features of the industrial continuous casting technique during the “soft reduction” stage (at the end of the solidification process), but the influence of the metallostatic pressure is neglected for simplicity. The main novelty of this work is the implementation of a modeling strategy that captures the dynamic effect of the contraction and dilatation states of the strand – which evolves during the casting process – in a simulation that considers a fixed geometry. The goal is to develop a valid numerical framework that does not use a pre-defined strand deflection profile, since it directly influences the outcome of the simulation, while still considering the effect of mush deformation and solidification kinetics in the casting outcome.

2. Model description

2.1. General conservation equations

A two-phase Eulerian–Eulerian volume-average model is used in this study. It solves the volume-average conservation equations of mass, momentum, species, and enthalpy (as shown in Table 1) for two phases: solid equiaxed crystals (s) and liquid melt (ℓ). The sum of their volume fractions always equals unity. An extra transport equation for the number density of the equiaxed crystals is also considered (Eq. 5). Note that all symbols are defined in the Nomenclature.

The new enthalpy is used to update the temperature using the following thermodynamic relation: $h_i = \int_0^{T_i} c_{p,i} dT$. The latent heat is considered implicitly in the model as the difference between the enthalpies of the two phases (note that the heat capacity is different for each phase). $M_{\ell s}$, $U_{\ell s}$, $C_{\ell s}$, and $H_{\ell s}$ are the source terms for the conservation equations of mass,

Table 2
Source terms in the conservation equations.

Mass transfer rate:	$M_{\ell s} = v_r S_{\ell s} \rho_s \phi_{\text{imp}}$	(6)
Momentum transfer rate:	$U_{\ell s} = U_{\ell s}^d + u^* M_{\ell s}$	(7)
Species transfer rate:	$C_{\ell s} = c_s^* M_{\ell s}$	(8)
Enthalpy transfer rate:	$H_{\ell s} = h_c (T_\ell - T_s)$	(9)

Table 3
Variables in the mass transfer rate equation.

Interfacial growth velocity:	$v_r = \frac{D_i}{r_i(1-r/r_i)} \frac{c_\ell^* - c_\ell}{c_\ell^*(1-k)}$	(10)
Specific surface area:	$S_{\ell s} = n \cdot 4\pi r^2$	(11)
Impingement factor:	$\phi_{\text{imp}} = \min[g_\ell / (1 - \pi\sqrt{3}/8), 1]$	(12)

momentum, species, and energy, respectively. They take the negative sign in the liquid phase and positive sign in the solid phase. They are presented in Table 2.

In Eq. (9), $h_c = 10^9 \text{ W}/(\text{m}^3 \cdot \text{K})$. This large value guarantees that both phases have a similar temperature. In $M_{\ell s}$, v_r is the interfacial growth velocity of the equiaxed crystals, $S_{\ell s}$ is the specific surface area of the equiaxed crystal, and ϕ_{imp} is the impingement factor. They are defined in Table 3.

Note that $(c_\ell^* - c_\ell)$ is the driving force for the solidification/remelting. When $(c_\ell^* - c_\ell) > 0$, $v_r > 0$ which means solidification occurs, whereas when $(c_\ell^* - c_\ell) < 0$ remelting occurs. The equilibrium species concentration in the liquid phase at the interface (c_ℓ^*) can be obtained by Eqn. (13).

$$c_\ell^* = (T_\ell - T_{\text{liq}}) / m_{\ell s} \tag{13}$$

2.2. The viscoplastic model

For the effective viscous stress term in the momentum equation, a viscoplastic model is considered when the solid fraction is above a viscoplastic threshold ($g_s^t = 0.57$) [13]. This means that above this threshold, the solid skeleton is coherent enough to sustain high stresses. Under the viscoplastic threshold or in the liquid phase, the stress term is a function of the deviatoric part of the strain rate. This is summarized in Eqs. (14) and (15).

$$\text{Liquid phase : } \tau_\ell^{\text{eff}} = 2\mu_\ell \text{dev}(\dot{\epsilon}_\ell) \tag{14}$$

$$\text{Solid phase : } \tau_s^{\text{eff}} = \begin{cases} 2\mu_s \text{dev}(\dot{\epsilon}_s) & \text{for } g_s \leq g_s^t \\ 2\frac{\mu_s^{\text{app}}}{A} \text{dev}(\dot{\epsilon}_s) + \mu_s^{\text{app}} \left(\frac{1}{9B}\right) \text{tr}(\dot{\epsilon}_s) \mathbf{I} & \text{for } g_s > g_s^t \end{cases} \tag{15}$$

In Eqs. (14) and (15), $\dot{\epsilon}_\ell$ and $\dot{\epsilon}_s$ are the strain-rate tensors of the liquid and solid phases, respectively, \mathbf{I} is the identity tensor, μ_ℓ is the constant liquid viscosity, and μ_s is the solid viscosity given by the following equation:

$$\mu_s = \frac{\mu_\ell}{g_s} \left(\left(1 - \frac{g_s}{g_s^p} \right)^{-2.5g_s^p} - (1 - g_s) \right) \tag{16}$$

The packing limit (g_s^p) is equal to 0.585, according to Olmedilla’s work [25]. In the viscoplastic regime, μ_s^{app} is the apparent solid viscosity which takes the form given in the Norton–Hoff model [26]:

$$\mu_s^{\text{app}} = 3K_v (\sqrt{3}\dot{\epsilon}_s^{\text{eq}})^{m-1} \tag{17}$$

where K_v is the viscoplastic consistency, which is equal to $6.31 \times 10^6 \text{ Pa} \cdot \text{s}$ [23], and m is the strain-rate sensitivity constant, which is equal to 0.213 [13]. In Eq. (17), the equivalent strain rate ($\dot{\epsilon}_s^{\text{eq}}$) can be written as follows:

$$\dot{\epsilon}_s^{\text{eq}} = \sqrt{\frac{2}{A} (\dot{\epsilon}_s : \dot{\epsilon}_s) - \left(\frac{2}{3A} - \frac{1}{9B} \right) \text{tr}(\dot{\epsilon}_s)^2} \tag{18}$$

For the Al-4 wt pct. Cu alloy, the rheological parameters of A and B are shown in Eqs. (19) and (20) [13,23].

$$A = 3/g_s^{6.47} \tag{19}$$

$$B = 9 \times 10^{-3} (1/g_s^{6.94} - 1) \tag{20}$$

Further details of the viscoplastic model can be found in Rodrigues et al. [22].

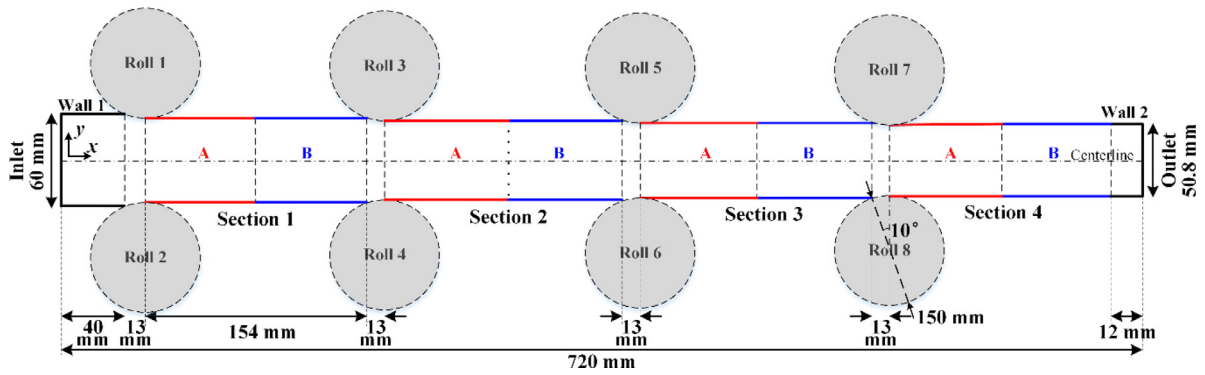


Fig. 1. Schematic representation of the geometry and calculation domain. At each pair of rolls, the slab reduction is 2.3 mm.

Table 4

Discretization schemes for each term of the conservation equations (ψ refers to a generic variable).

Term	Discretization schemes
$\partial/\partial t$	Euler implicit
$\nabla\psi$	Gauss linear
$\nabla \cdot (\mathbf{v}_i\alpha_i)$	Gauss vanLeer
$\nabla \cdot (\mathbf{v}_i\mathbf{v}_i)$	Gauss limitedLinearV 1
$\nabla \cdot (\mathbf{v}_i\alpha_i\psi)$	Gauss limitedLinear 1
$\nabla \cdot (\psi)$	Gauss linear
$\nabla^2\psi$	Gauss linear corrected
$(\psi)_f$	linear

3. Numerical implementation

3.1. Model geometry

The model has been developed within the OpenFOAM software framework (version 5.0). The schematic diagram of the geometry used in this work is shown in Fig. 1. The geometry replicates an octuplet-roll casting technique, which subjects the strand to successive regions of MR and rolling. The length of the total calculation domain is 720 mm, the initial height is 60 mm, the roll diameters are 150 mm, and the distance between rolls in each section is 154 mm. At each roll pair, the slab reduction is 2.30 mm. The whole calculation domain is 2D and is divided into 1440 quadrilaterals cells (i.e., 96 in the horizontal direction and 15 in the vertical direction). Each section contains 300 cells, with 20 cells along the horizontal direction (10 in red section and 10 in blue section). The time step size was set at 1×10^{-6} s. The steady state was reached after 125 s. The results were independent of mesh resolution (meshes with two and four times more cells than the current one were tested).

The solution algorithm is based on the PIMPLE approach. The numerical configuration adopted in the simulations uses predominantly linear solvers with Gauss–Seidel smoothers [27]. The exception is the pressure field which is solved using a geometric–algebraic multigrid solver, with a (symmetric) diagonal incomplete–Cholesky smoother [27]. The numerical schemes used to discretize each term in the conservation equations are summarized in Table 4. For the source terms of the mass, momentum, energy and solute conservation equations, an implicit treatment was adopted to improve the robustness of the model [23].

3.2. Boundary conditions

The main boundary conditions used in the simulations are listed in Table 5. The location of each patch can be found in Fig. 1. At the “Inlet”, a static pressure value of 10^5 Pa has been assumed, so that the velocity of the flow is adjusted according to the downstream solution. All the remaining patches have zero Neumann boundary conditions for pressure. At the “Outlet”, the casting speed of 0.012 m/s was set. At “Wall 1” and “Wall 2”, a no-slip velocity boundary condition was applied to the liquid phase, whereas a slip velocity boundary condition was applied to the solid phase. Similarly, at the rolls, an angular velocity (between 0.14 rad/s and 0.16 rad/s depending on the strand thickness) was assumed for the liquid phase, whereas a slip boundary condition was assumed for the solid. Between each pair of rolls (Sections 1 to 4), the strand surface is divided into sub-domain A and B, which have their special set of Robin type boundary conditions. A detailed description of these boundary conditions is given in section 3.D.

Table 5
Boundary conditions for velocity and temperature fields.

Patch		Velocity/Pressure liquid	solid	Temperature(liquid and solid)	Species/Number density (liquid and solid)
Inlet		Fixed pressure (10 ⁵ Pa)	Fixed pressure (10 ⁵ Pa)	Fixed temperature (919.74 K)	Fixed value (same as initial values)
Outlet		Fixed velocity (0.012 m/s 0 0)	Fixed velocity (0.012 m/s 0 0)	Zero Gradient	Zero Gradient
Wall 1		No slip	Free slip	Fixed temperature (919.74 K)	Zero Gradient
Section 1	Sub-domain A	Custom BC1		Heat Flux (T [∞] = 300 K, h _c = 4300 W/m ² /K)	Zero Gradient
	Sub-domain B	Custom BC2		Heat Flux (T [∞] = 300 K, h _c = 4300 W/m ² /K)	Custom BC2
Section 2, 3, 4	Sub-domain A	Custom BC1		Heat Flux (T [∞] = 300 K, h _c = 100 W/m ² /K)	Zero Gradient
	Sub-domain B	Custom BC2		Heat Flux (T [∞] = 300 K, h _c = 100 W/m ² /K)	Custom BC2
Wall 2		No slip	Free slip	Heat Flux (T [∞] = 300 K, h _c = 100 W/m ² /K)	Zero Gradient
Rolls 1, 2		Rotating velocity (0.14-0.16 rad/s)	Free slip	Heat Flux (T [∞] = 300 K, h _c = 4300 W/m ² /K)	Zero Gradient
Rolls 3-8		Rotating velocity (0.14-0.16 rad/s)	Free slip	Heat Flux (T [∞] = 300 K, h _c = 600 W/m ² /K)	Zero Gradient

Table 6
Initial conditions and thermodynamic properties for Al-4wt pct. Cu [23].

	Item	Value
Initial conditions	Temperature of pure Al, T _{liq}	933.5 K
	Initial solid fraction, f _s	1 × 10 ⁻⁵
	Initial temperature (liquid, solid), T _l /T _s	919.74 K/919.74 K
	Liquid species mass fraction, c _l	0.04 wt pct.
	Solid species mass fraction, c _s	0.0058 wt pct.
	Number density of equiaxed crystals, n	1.53 × 10 ¹¹ m ⁻³
Thermodynamic properties	Liquidus slope, m _{ls}	-3.44 K.(wt pct.) ⁻¹
	Redistribution coefficient, k	0.145
	Density (liquid, solid), ρ _l /ρ _s	2606/2743 kg/m ³
	Viscosity (liquid), μ _l	0.013 kg/m/s
	Thermal conductivity (liquid, solid), λ _l /λ _s	77/153 W/m/K
	Heat capacity (liquid, solid), c _{p(l)} /c _{p(s)}	1179/766 J/kg/K
	Diffusion coefficient (liquid, solid), D _l /D _s	5 × 10 ⁻⁹ /8 × 10 ⁻¹³ m ² /s

Heat flux boundary conditions were applied on the slab surfaces and rolls: the cooling temperatures and corresponding values for the heat transfer coefficient (h_c) are given in Table 5. Note that, at the beginning of the domain (i.e., in Section 1 and in the first pair of rolls), exaggerated cooling conditions have been imposed to expedite the solidification process and quickly reach a kissing point. The remaining sections assume more moderate cooling conditions. As it will be shown later, this allows us to analyze, in a smaller test case, regions of the process where melt is expected to still separate the two solid shells (Section 1) and regions of the process where the semi-solid has a fully viscoplastic behavior in between rolls (Sections 3 and 4).

The simulation starts with a very small solid fraction of 1 × 10⁻⁵ (not absolute 0 for numerical reasons), and a casting temperature of 919.74 K (i.e., slightly above liquidus temperature, T_{liq}). The alloy used in this simulation is Al-4 wt pct. Cu. The initial equiaxed crystal radius is r = 2.5 × 10⁻⁶ m and the initial number density is given by the geometrical relation n = f_s / ((4π/3) · r³). The initial conditions and thermodynamic properties for Al-4 wt pct. Cu are listed in Table 6.

3.3. Modelling strategy for contraction/dilatation states between rolls in fixed geometry

Fig. 2 compares the current modeling strategy (Fig. 2b) with the standard solution (Fig. 2a) adopted in the literature to model the contraction/dilatation states between rolls in a fixed geometry. In both cases, each section between the two rolls is divided into two sub-domains: sub-domain A and sub-domain B.

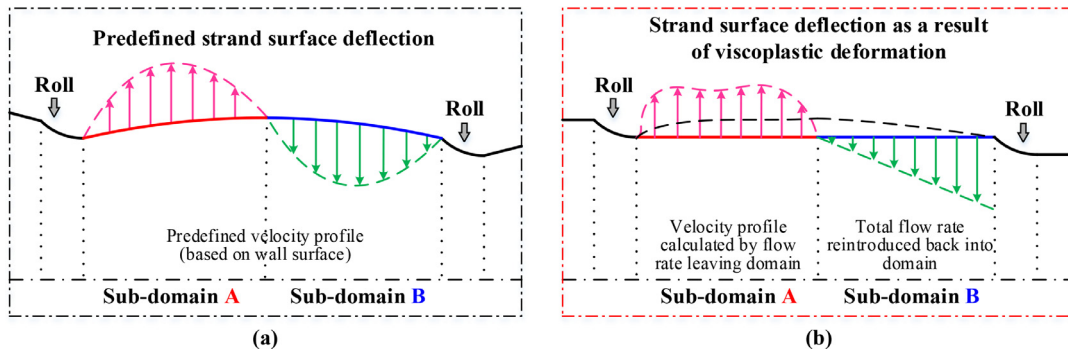


Fig. 2. Comparison between different modeling strategies used to model contraction/dilatation between rolls: (a) with predefined strand deflection [28], and (b) with strand deflection as a result of viscoplastic deformation during MR (present work).

In Fig. 2a, the approach is based on the work of Miyazawa and Schwerdtfeger [18] and later adopted by Domitner et al. [28]. It assumes that the strand surface deflection has a fixed pattern that can be approximated with a cosine function. The velocity is determined based on the derivative of the given curve and no solid deformation is considered.

In Fig. 2b, the approach adopted in the current work considers the viscoplastic behavior of the mush, and the strand has straight surfaces between rolls. During MR, the pressing forces from the rolls on the viscoplastic body leads to the compression of the semi-solid material inside the mushy zone, which causes liquid to be squeezed out of the solid skeleton. If this liquid flow is strong enough to go through the solid shell and reach the strand surface in sub-domain A, it is assumed that its inertia is able to deflect the strand in that region. Numerically, the liquid flow is allowed to leave the domain through the surfaces of sub-domain A. This corresponds to the dilatation state. In sub-domain B, the total calculated outflow is then re-introduced back into the domain to fulfill mass conservation. As a result, the strand surface deflects back to its original form as the fixed support of the following pair of rolls approaches. This corresponds to the contraction state. The potential strand deflection between two pair of rolls is estimated based on the volumetric flow rate leaving sub-domain A and entering sub-domain B. Note that the solid and liquid densities are assumed to be different to each other, but constant (Table 6). Therefore, numerically, mass conservation is equivalent to volume conservation (see Appendix).

It is worth noting that strand surface deflection only takes place when $g_s > g_s^t$. If $g_s \leq g_s^t$, the solid skeleton is not coherent enough to sustain high stresses and so the contraction/dilatation states do not occur. Similarly, if liquid melt remains in between two coherent solid shells, the rolling pressure is damped by the liquid phase and no viscoplastic deformation takes place. Under such conditions, the patches in sub-domains A and B of Sections 1 to 4 are treated as free-slip walls. Furthermore, for simplicity, the metallostatic pressure influence is neglected in the current work, so that rolling pressure is the only origin of strand contraction/dilatation.

3.4. Custom boundary conditions in sub-domains A and B

If $g_s < g_s^t$, the strand surface behaves as a stationary wall in both sub-domains A and B. There is no strand deflection.

If $g_s \geq g_s^t$, for sub-domain A, the implementation relies on a Robin type boundary condition: (1) along the casting direction, the linear velocity is equivalent to the corresponding angular velocity of the preceding roll; and (2) normal to the casting direction, the outflow is treated using a Neumann boundary condition, whereas a possible inflow is treated with a fixed value of 0 (i.e., no reverse flow).

If $g_s \geq g_s^t$, for sub-domain B, the implementation also relies on a Robin type boundary condition: (1) along the casting direction, the velocity on the patch of sub-domain B is equal to the mean velocity obtained on the patch of sub-domain A (see Eq. (21)); and (2) normal to the casting direction, a uniform velocity field is firstly determined to match the flow rate calculated in sub-domain A and then the velocity field is adapted to give a pre-defined profile along the patch of sub-domain B (see Eq. (22)).

As mentioned above, along the casting direction, the average velocity in sub-domain B is calculated as follows:

$$v_{i,x}^B = \frac{\sum (v_{i,x}^A)}{N_{cell}^A} \tag{21}$$

where the superscripts A and B represent the corresponding sub-domains, the subscript x represents the x -component of the velocity, the subscript i represents the solid or liquid phase, and N_{cell}^A is the total number of cells on the surface of sub-domain A.

Normal to the casting direction, in sub-domain B, the following expression has been used:

$$v_{i,y}^B = 2 \frac{N_{celli}^B}{N_{cell}^B} \frac{\sum (\phi_{f(i)}^A)}{S_f^A} \tag{22}$$

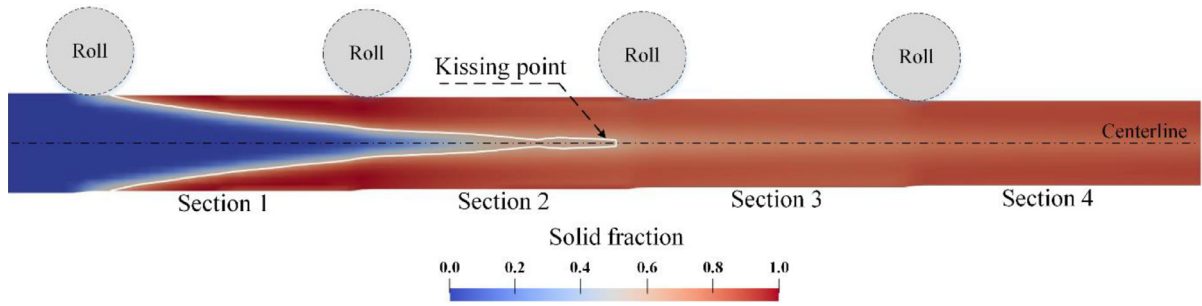


Fig. 3. Steady-state result for solid fraction. The white line represents the viscoplastic threshold.

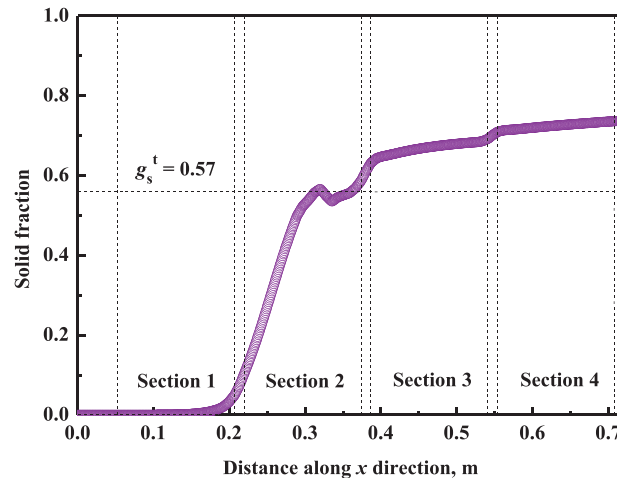


Fig. 4. Steady-state result for solid fraction along the centerline. The horizontal dashed line represents the viscoplastic threshold. The vertical dotted lines represent the position of the rolls.

where the factor 2 comes from the triangle similarity theorem, $\sum(\phi_{f(i)}^A)$ is the sum of the volumetric flow through the entire patch in sub-domain A, S_f^A is the total patch area in sub-domain A, N_{celli}^B represents the cell number along the patch of sub-domain B, and N_{celli}^B is the total number of cells in the patch of sub-domain B. Eq. (22) gives a linear increase in velocity along the patch (like the profile shown in Fig. 2b). This profile is arbitrary and can be adjusted to better replicate the physics underlying strand deflection. This will be discussed in Section 5.B.

4. Results

4.1. Solid fraction distribution

Fig. 3 shows the solid fraction distribution in the domain. The intense cooling rates imposed in Section 1 produce rapid growing solid shells that are still separated by liquid melt at the centerline. After Section 1, normal cooling rates are assumed on the rolls and strand surface. As a result, the growth of the partly solid shells is more moderate, but they still merge before the end of Section 2 (i.e., kissing point). From this point, a fully coherent mush has been formed and so, according to the numerical implementation, the strand can now contract or dilate when subjected to MR in Sections 3 and 4.

The solid fraction evolution along the centerline is plotted in Fig. 4. It confirms that the solid fraction (g_s) surpasses the viscoplastic limit near the end of Section 2. After that, the more significant increases in solid fraction occur when the strand passes through each pair of rolls because of the relatively large imposed cooling conditions.

Although in Section 1 intense cooling conditions are imposed, the solid fraction is almost negligible in Fig. 4 because the line is taken along the centerline, where melt is still prevailing.

4.2. Velocity on the strand surface between rolls

Fig. 5(a1) and (b1) show the x- and y-components of the liquid velocity along the strand surface of Sections 1 to 4. The first half of each figure corresponds to sub-domain A, whereas the second half corresponds to sub-domain B.

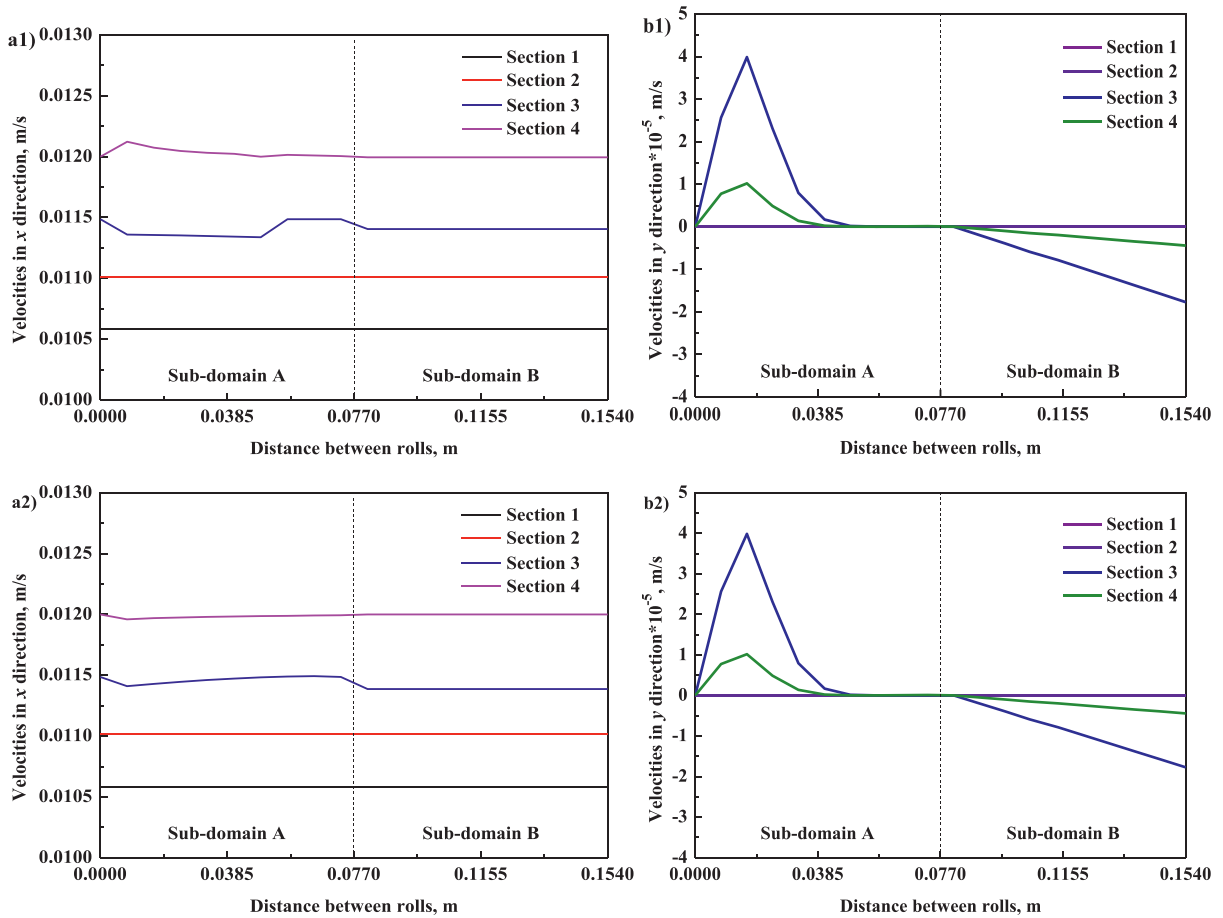


Fig. 5. Steady-state results of liquid (1) and solid (2) phases for (a) x-component, and (b) y-component of velocity along the strand surface between two rolls, for the four different sections considered.

In the x-component velocity plot (Fig. 5(a1)), increasingly larger liquid velocities are found in subsequent sections because of the decrease in strand thickness. The average x-component of the velocity in a particular section equates the radial velocity of the preceding roll. At Section 4, the average x-component of the liquid velocity corresponds to the casting speed imposed at the outlet (i.e., 12 mm/s).

The y-component of the liquid velocity is shown in Fig. 5(b1). Owing to the presence of melt in between the solid shells, the normal liquid velocities on the surface of Sections 1 and 2 are equal to 0 m/s. On the other hand, positive velocities normal to the strand surface are found in sub-domain A of Sections 3 and 4. The velocity magnitude reaches 40 $\mu\text{m/s}$ in Section 3 and 10 $\mu\text{m/s}$ in Section 4. In sub-domain B, owing to the contraction state, negative velocity curves (with constant negative slopes) are observed in both Sections 3 and 4. As expected, due to the larger outflow obtained in sub-domain A of Section 3, the equivalent average velocity in sub-domain B is larger in Section 3 than in Section 4.

During MR, deformation of the viscoplastic network causes liquid to be squeezed out of the solid skeleton. As shown in Fig. 5(b1), part of the flow moves towards the surface of the strand and leaves through sub-domain A. As the liquid moves, it starts to drag the solid structure with it and both phases tend to move with similar velocities relatively far from the deformation zone. This is demonstrated in Fig. 5(a2) and (b2), where the x- and y-components of the solid velocity along the strand surface between two rolls are presented. It can be seen that, along the strand surface, the solid phase has similar velocity curves as the liquid phase depicted in Fig. 5(a1) and (b1).

4.3. Estimated strand surface deflection between rolls

Fig. 6 shows the estimated normalized strand surface deflection between the rolls of Sections 3 and 4. The profiles are calculated by multiplying the outward solid velocity in each cell along the strand surface with a set period of time (in this case unity, for simplicity). In each cell, the calculated distance is summed over the distance calculated in the previous cell. This assumes that, once the velocity normal to the strand surface is non-zero, the strand surface has already been deflected

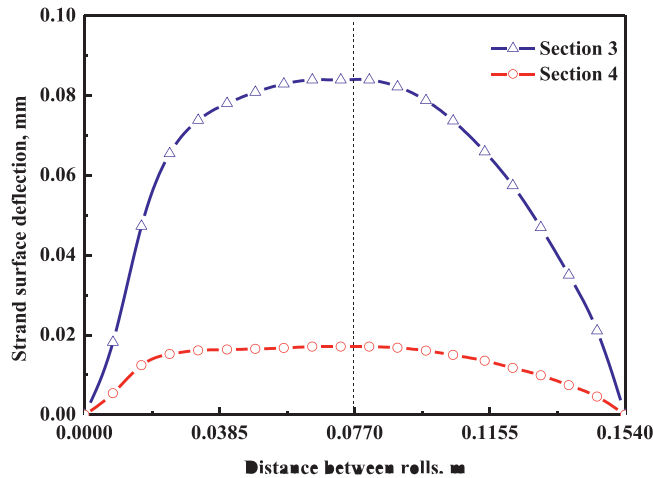


Fig. 6. Steady-state results for the estimated normalized strand surface deflection between rolls for Sections 3 and 4.

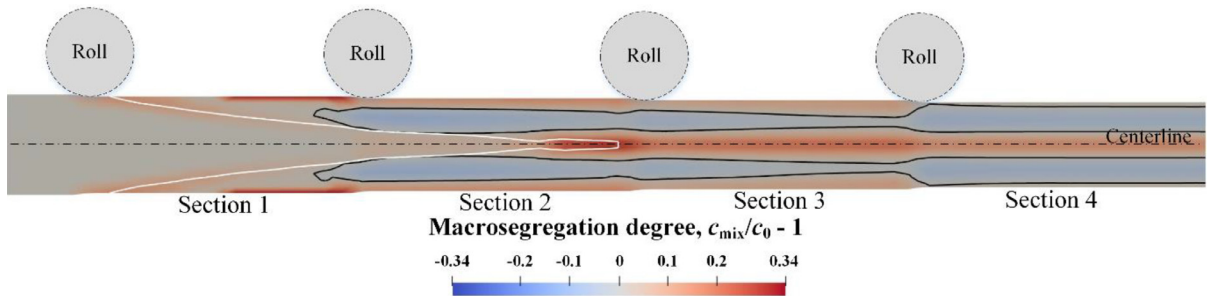


Fig. 7. Steady-state result for normalized macrosegregation. The black line represents $c_{mix}/c_0 - 1 = 0$. The white line represents the viscoplastic threshold.

and should be proportional to the normal velocity in this region. The idea is to compare qualitatively the potential deflection in two different sections based on the velocity of the solid phase on the surfaces between the rolls.

The maximum strand deflection in Section 4 is smaller than in Section 3 because it becomes increasingly more difficult for the flow to traverse the solid shell as solid fraction increases towards the end of the domain.

In Fig. 6, the first half of the curves is given by the time integral of the velocity profile from sub-domain A, which means that the strand dilatation is calculated directly from the outflow caused by the compression of the solid skeleton during MR. The second half of the curve (sub-domain B) in Fig. 6 is given by the time integral of the velocity profile defined in Eq. (22). As a result, the corresponding strand surface deflection becomes a parabola.

4.4. Macrosegregation distribution

Fig. 7 shows the distribution of the normalized macrosegregation for the present case. The macrosegregation pattern has been normalized ($c_{mix}/c_0 - 1$) so that the initial alloy composition is given by the value 0, whereas positive or negative macrosegregation is illustrated with positive or negative values, respectively.

In Section 1, after passing the first pair of rolls, a slightly positive macrosegregation forms, which progresses away from the wall, in front of the solid shell (see Fig. 3). Then, closer to the second pair of rolls (before Section 2), a positive macrosegregation is predicted near the strand surface. After entering Section 2, a positive macrosegregation can be identified along the slab centerline, particularly near the kissing point, where a significant positive macrosegregation region arises. Near the strand surface, macrosegregation has slightly larger values than in the neighboring inward regions, which is called “inverse macrosegregation” [29]. In between the strand surface and the centerline, negative macrosegregation can be seen.

Fig. 8 shows that the steady-state results for the normalized macrosegregation ($c_{mix}/c_0 - 1 \times y$) along the vertical direction (y axis) at $x = 0.7$ m (in Section 4). The integral of $c_{mix}/c_0 - 1$ is very close to 0, which means that solute is conserved during the simulation.

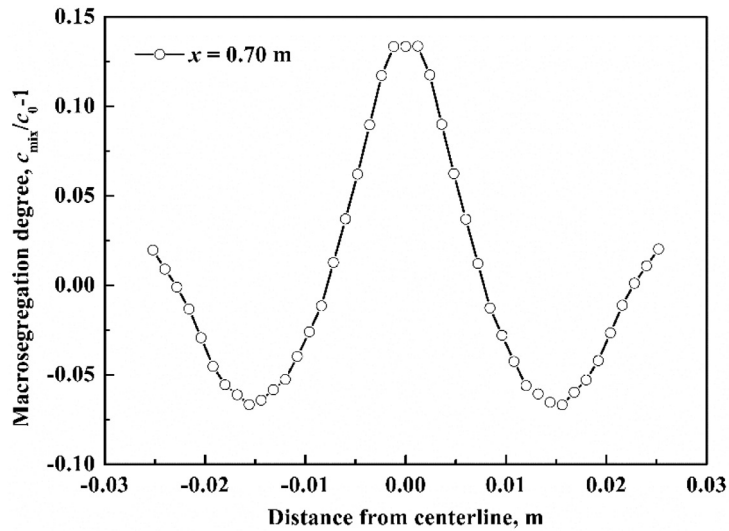


Fig. 8. Steady-state results for the normalized macrosegregation along the vertical direction (y axis) at $x = 0.7$ m.

Table 7

Difference between volumetric flow rate leaving and entering sub-domains A and B.

Sections	Difference
1	0 m ³ /s
2	0 m ³ /s
3	1.5146×10^{-9} m ³ /s
4	3.7917×10^{-10} m ³ /s

5. Discussion

5.1. Mass conservation analysis

The current modeling strategy has been devised to capture the strand contraction/dilatation state in a fixed geometry. It employs Robin type boundary conditions in the patches between the rolls. It is thus critical to make sure that mass is conserved in the system.

Mass conservation has been tested between sub-domains A and B for all the patches where the custom boundary conditions have been implemented. The difference between the volumetric flow rate leaving sub-domains A and entering sub-domains B in each section is shown in Table 7. Note that the model assumes constant densities in both phases, so the volumetric flow rate parameter is employed in this analysis. The results are obtained after the simulation reaches a steady-state solution, at $t = 145$ s.

In Sections 1 and 2, the difference is equal to zero because viscoplastic deformation does not occur and the patches between rolls behave as walls. In Sections 3 and 4, the difference is under 1.5146×10^{-9} m³/s, which is below computer round-off and iterative convergence errors. Both solute and number density conservations have also been confirmed over the custom boundary conditions.

5.2. Strand surface deflection analysis

The velocity profile at the strand surface along sub-domain A is directly obtained from the local volumetric flow rate of the solid phase calculated in that patch. This means that the strand deflection estimation is a direct reflection of the mush deformation during MR. A large deformation intensity in Section 3 leads to a large deflection. The deflection magnitude reduces as solidification progresses.

On the other hand, in sub-domain B, the velocity is reconstructed from the average total flux obtained in sub-domain A. Without any changes, this would result in a constant velocity inflow in sub-domain B, which would cause a linear strand surface deflection (with negative constant slope). This does not seem plausible. As a result, in this work, the velocity inflow in sub-domain B has been set with a linear function, as explained in Eq. (22), and shown in Fig. 5(b2). This results in a parabola for the strand surface deflection, as shown on the second half of Fig. 6. Note that the length ratio between sub-

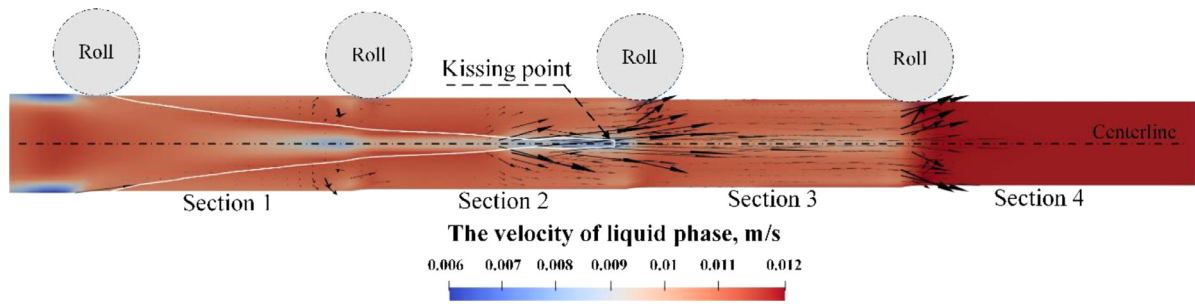


Fig. 9. Steady-state result of the liquid velocity in the x direction. The arrows represent the relative velocity between solid and liquid.

domains A and B can be changed in the current approach. Here, for the sake of simplicity, the length ratio has been kept to 1 (i.e., both patches have the same length).

Overall, the strand deflection profiles shown in Fig. 6 seem to agree with the deflection profile generally assumed in the literature [18,21,28]. This is achieved without the need to enforce a strand deflection profile as a boundary condition. Even when larger strand deformations take place, the profiles seem to maintain a similar trend. Even though currently the strand deflection is only originated from MR, the model can be extended to capture the bulging phenomena that occurs when the metallostatic pressure present in continuous casting processes is considered. Nevertheless, further research should be done in this area to validate the present model.

5.3. Liquid and relative velocity results

In Fig. 9, the steady-state results of the x-component of the liquid velocity are illustrated. The light blue areas along the centerline, before each pair of rolls, reveal that the liquid velocity along the casting direction reduces considerably each time they approach a pair of rolls. This is also consistent with the black arrows shown in Fig. 9, which represent the relative velocity between the solid and the liquid phases.

Two mechanisms are behind the blue regions. Before a fully coherent mush has emerged (i.e. Sections 1 and 2), the growth of the solid shell into a smaller domain (i.e. MR under each pair of rolls) leads to a relative motion between the two phases where the liquid phase slows down as the solid shells approach each other in the center. After a coherent mush has been formed (i.e. Sections 3 and 4), compression-induced squeezing out of melt during mush deformation occurs. In this case, melt is pressed out of the solid skeleton. This flow is mostly directed upstream, along the centerline, which is where solid fraction is typically lower. As a result, the black arrows before each pair of rolls point downstream, which indicates that the x-component of the velocity of the solid phase is larger than the x-component of the velocity of the liquid phase. The liquid velocity value is still positive (light blue areas) because the casting is moving downstream with a larger velocity. This phenomenon requires the strand to be totally in the viscoplastic regime, and thus does not occur before the 3rd pair of rolls where melt is still present in between the solid shells (Fig. 3).

In Fig. 9, black arrows are also observed pointing towards the strand surface under the 3rd and 4th pair of rolls. This demonstrates that, during the compression of the solid skeleton, the melt is not only squeezed out upstream (in relation to the overall casting speed), but some melt also travels through the coherent network towards the strand surface. This results in the strand dilatation state discussed above. Closer to the strand surface, the arrows disappear because the melt drags the solid until they move with the same speed.

5.4. Understanding mush deformation

The mush deformation can be analyzed by taking the divergence of the solid velocity. A negative divergence of the solid velocity indicates that the solid skeleton in the mushy zone is compressing. As a result, solute-rich melt is expelled out of the region and negative segregation appears locally. On the other hand, a positive divergence of the solid velocity indicates the expansion of the solid skeleton, which is reflected by the inflow of solute-rich melt locally and a positive segregation. This is schematically illustrated in Fig. 10.

Steady-state results of the divergence of the solid velocity are presented in Fig. 11. The black and white lines represent the zero solid divergence and the viscoplastic threshold, respectively. Under the 1st pair of rolls, and in front of the solid shell, a blue area can be identified, which means that the divergence of the solid velocity is negative. This is due to the intense solidification occurring under the first pair of rolls and in Section 1, which creates a solid shell growing towards the centerline and a melt feeding flow directed towards the solid shell. As a result, positive segregation develops at the edge of the solid shell, as shown in Fig. 7.

The red zone highlighted in the insert of Fig. 11 corresponds to a positive divergence of the solid velocity as a result of expansion of the solid skeleton. This zone indicates that an influx of melt occurred locally. In this case, the influx of melt is due to the compression of the solid skeleton, which drives solute-rich melt upstream (in relation to the casting speed). This

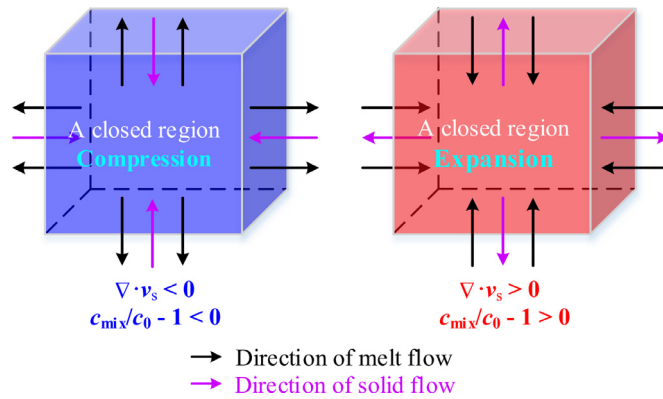


Fig. 10. Effect of solid deformation on the divergence of solid velocity and on macrosegregation.

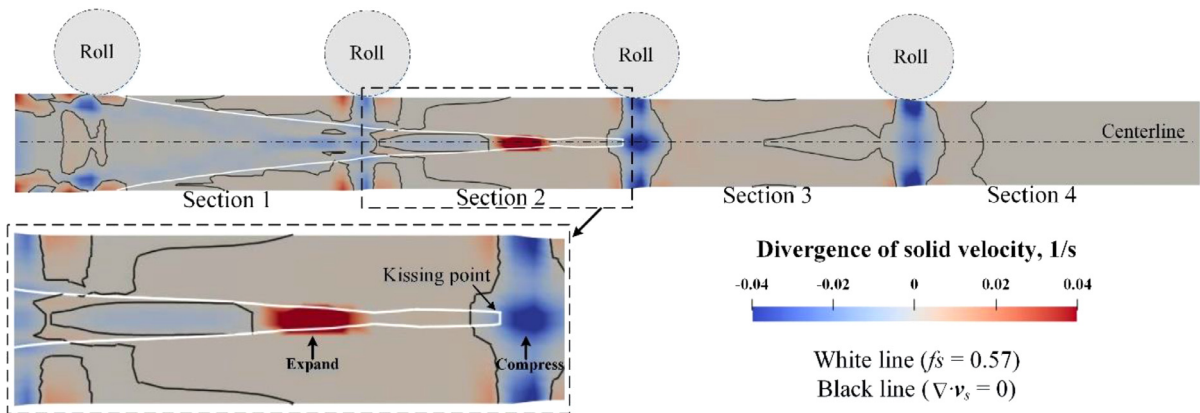


Fig. 11. Steady-state results of the divergence of the solid velocity.

is supported by the relative arrows shown in Fig. 9 and the intense centerline positive macrosegregation observed before the 3rd pair of rolls in Fig. 7. As the casting continues to move downstream, this positive macrosegregation continues, until a new compression zone appears under the 4th pair of rolls, where a similar mechanism occurs.

Under both the 3rd and 4th pair of rolls, negative solid velocity divergence zones are found, which means compression of the solid skeleton. This is due to the pressing forces of the rolls during MR. The negative solid velocity divergence is greater in the 3rd pair of rolls than in the 4th, which supports the strand surface deflection difference estimated in Fig. 6. In between the rolls, the solid velocity divergence is initially positive (which means expansion of the solid skeleton) right after the 3rd pair of rolls, and then decreases as it approaches the following pair of rolls and becomes negative again (as identified by the black line). This agrees with the strand dilatation/contraction mechanism discussed before. This successive alternation between negative (under the rolls) and positive (between the rolls) solid velocity divergence was also reported in Fachinotti et al. [21] in their final distribution results.

6. Conclusion

The strand deflection induced by solid deformation during MR has been modelled by means of a two-phase Eulerian–Eulerian volume-average model with fixed mesh. The conclusions are as follows:

- (1) The modeling strategy used to account for the contraction/dilatation state during MR in a fixed geometry seems to produce plausible results for the setup considered here.
- (2) The magnitude of the strand deflection underlying the contraction/dilatation states correlates well with the divergence of the solid velocity and magnitude of the mush deformation during the casting process.
- (3) The maximum strand deflections in Section 3 and Section 4 are 0.08 mm and 0.015 mm, respectively. The maximum strand deflection in Section 4 is smaller than in Section 3 because the shell is harder to deform when the solid fraction increases. This means that the deflection magnitude reduces as solidification progresses.
- (4) Due to the deformation of the solid skeleton during MR, a positive centerline macrosegregation has been found, which is due to the compression-induced squeezing out of solute-rich melt against casting direction, along the centerline. This is particularly significant when, upstream of the compression zone, the solid fraction is under the viscoplastic regime.

- (5) The negative divergence of solid velocity indicates that the solid skeleton in the mushy zone is compressing. As a result, solute-rich melt is expelled out of the region and negative segregation appears locally. On the other hand, positive divergence of solid velocity indicates the expansion of the solid skeleton, which is reflected by the inflow of solute-rich melt locally and a positive segregation. Such results support the understanding of the macrosegregation distribution, as well as the strand deflection states.

The present model has been analyzed in a simplified geometry that accounts for strand deflection as a result of the deformation of the dendritic network during MR. However, it can be easily extended to more practical applications, such as continuous casting of steel, where bulging due to metallostatic pressure also plays a big role on the outcome. Furthermore, there is still a need to validate the model against experimental results, although this is difficult to achieve due to the scarcity of the available data. This should not detract from the current work, which is meant to add a novel numerical framework by which new studies can be carried out on strand deflection and bulging, thereby adding to the limited understanding in the topic.

Data Availability

Data will be made available on request.

Acknowledgments

This work was financially supported by the FWF Austrian Science Fund (P28785-N34), the National Natural Science Foundation of China U1560208, and Fundamental Research Funds for the Central Universities of China N172504024 and N182515006. The author RG acknowledges the financial support from the China Scholarship Council (No.201906080127), and the main work was accomplished during his stay at the Montanuniversitaet Leoben, Austria. The authors acknowledge the financial support by the Austrian Federal Ministry of Economy, Family and Youth and the National Foundation for Research, Technology and Development within the framework of the Christian Doppler Laboratory for Metallurgical Applications of Magnetohydrodynamics.

Appendix

The definition of volumetric flow rate

For the finite volume method (FVM), the flow rate on the face of each cell is the most fundamental parameter, which can participate in the calculation for solving the conservation equations of mass, momentum, species, and enthalpy in this work. Taking the momentum conservation equation as an example, the role of flow rate in the calculation process is illustrated as follows. Firstly, to use the finite volume method, the momentum equation needs to be written in integral form, as shown in Eq. (A1).

$$\int_V \left[\frac{\partial (g_i \rho_i v_i)}{\partial t} + \nabla \cdot (g_i \rho_i v_i v_i) \right] dV = \int_V [-g_i \nabla p + \nabla \cdot (g_i \tau_i^{eff}) \mp U_{is}] dV \tag{A1}$$

In Eq. (A1), the term of $\int_V [\nabla \cdot (g_i \rho_i v_i v_i)] dV$ is further analyzed. According to the Gauss theorem, the surface integral of the physical quantity on the cell face is equal to the volume integral of the divergence of the physical quantity in the volume enclosed by the cell face. So, the term of $\int_V [\nabla \cdot (g_i \rho_i v_i v_i)] dV$ in Eq. (A1) can be transformed into $\oint_{\partial V} (g_i \rho_i v_i v_i) \cdot dS$. The dS is the infinitesimal area vector. Because a volume cell is always made up of a finite number of faces, the term of $\int_V [\nabla \cdot (g_i \rho_i v_i v_i)] dV$ in Eq. (A1) can be further defined, as shown in Eq. (A2).

$$\int_V [\nabla \cdot (g_i \rho_i v_i v_i)] dV = \oint_{\partial V} (g_i \rho_i v_i v_i) \cdot dS = \sum_f \int_{S_f} (g_i \rho_i v_i v_i) \cdot dS_f = \sum_f (g_i \rho_i v_i v_i)_f \cdot S_f \tag{A2}$$

Here, S_f is the area vector for one volume cell. The term of $(g_i \rho_i v_i v_i)_f$ is derived as follows.

$$(g_i \rho_i v_i v_i)_f = \frac{1}{\text{mag}(S_f)} \int_{S_f} (g_i \rho_i v_i v_i) \cdot dS_f \tag{A3}$$

where

$$(g_i \rho_i v_i v_i)_f \approx ((g_i \rho_i)_f (v_i)_f (v_i)_f) \tag{A4}$$

Then, the Eq. (A2) is approximated as follows.

$$\sum_f (g_i \rho_i v_i v_i)_f \cdot S_f \approx \sum_f ((g_i \rho_i)_f (v_i)_f (v_i)_f) \cdot S_f \tag{A5}$$

Finally, the Eq. (A5) can be further expressed as follows.

$$\begin{aligned} \sum_f ((g_i \rho_i)_f (v_i)_f (v_i)_f) \cdot S_f &= \sum_f ((g_i \rho_i)_f (v_i)_f ((v_i)_f \cdot S_f)) \\ &= \sum_f ((g_i \rho_i)_f (v_i)_f \phi_{f(i)}) \end{aligned} \quad (\text{A6})$$

Here, the $\phi_{f(i)}$ is the volumetric flow rate for each phase, $\sum_f ((v_i)_f \phi_{f(i)})$ is the sum of the product of the flow rate and the velocity on the face contained in each cell. Therefore, the volumetric flow rate ($\phi_{f(i)}$), as a most fundamental parameter, can be extracted and utilized in this work to realize the development of boundary conditions.

References

- [1] S.M. Cho, B.G. Thomas, Electromagnetic effects on solidification defect formation in continuous steel casting, *JOM* 72 (2020) 3610–3627, doi:[10.1007/s11837-020-04329-8](https://doi.org/10.1007/s11837-020-04329-8).
- [2] V.R. Voller, A.D. Brent, C. Prakash, The modelling of heat, mass and solute transport in solidification systems, *Int. J. Heat Mass Transf.* 32 (1989) 1719–1731, doi:[10.1016/0017-9310\(89\)90054-9](https://doi.org/10.1016/0017-9310(89)90054-9).
- [3] A. Ludwig, M. Wu, A. Kharicha, On macrosegregation, *Metall. Mater. Trans. A* 46 (2015) 4854–4867, doi:[10.1007/s11661-015-2959-4](https://doi.org/10.1007/s11661-015-2959-4).
- [4] A. Ludwig, M. Wu, Modeling of globular equiaxed solidification with a two-phase approach, *Metall Mater Trans A* 33 (2002) 3673–3683, doi:[10.1007/s11661-002-0241-z](https://doi.org/10.1007/s11661-002-0241-z).
- [5] M.C. Flemings, Our understanding of macrosegregation: past and present, *ISIJ Int.* 40 (2000) 833–841, doi:[10.2355/isijinternational.40.833](https://doi.org/10.2355/isijinternational.40.833).
- [6] W. Bennon, F. Incropera, A continuum model for momentum, heat and species transport in binary solid-liquid phase change systems—I. Model formulation, *Int. J. Heat Mass Transf.* 30 (1987) 2161–2170.
- [7] W. Bennon, F. Incropera, The evolution of macrosegregation in statically cast binary ingots, *Metall. Mater. Trans. B* 18 (1987) 611–616.
- [8] J. Ni, C. Beckermann, A volume-averaged two-phase model for solidification transport phenomena, *Metall. Mater. Trans. B* 22 (1991) 349–361.
- [9] C. Beckermann, R. Viskanta, Mathematical modeling of transport phenomena during alloy solidification, *Appl. Mech. Rev.* 46 (1993) 1–27.
- [10] D.R. Poirier, P.J. Nandapurkar, S. Ganesan, The energy and solute conservation equations for dendritic solidification, *Metall. Trans. B* 22B (1991) 889–900.
- [11] M. Wu, A. Ludwig, A three-phase model for mixed columnar-equiaxed solidification, *Metall. Mater. Trans. A* 37 (2006) 1613–1631.
- [12] H. Combeau, M. Založnik, S. Hans, P.E. Richey, Prediction of macrosegregation in steel ingots: influence of the motion and the morphology of equiaxed grains, *Metall. Mater. Trans. B* 40B (2009) 289–304.
- [13] T.G. Nguyen, D. Favier, M. Suéry, Theoretical and experimental study of the isothermal mechanical behaviour of alloys in the semi-solid state, *Int. J. Plast.* 10 (1994) 663–693, doi:[10.1016/0749-6419\(94\)90028-0](https://doi.org/10.1016/0749-6419(94)90028-0).
- [14] L. Martin, D. Favier, M. Suéry, Fracture behaviour in tension of viscoplastic porous metallic materials saturated with liquid, *Int. J. Plast.* 15 (1999) 981–1008, doi:[10.1016/S0749-6419\(99\)00017-0](https://doi.org/10.1016/S0749-6419(99)00017-0).
- [15] L. Martin, M. Braccini, M. Suéry, Rheological behavior of the mushy zone at small strains, *Mat. Sci. Eng. A* 325 (2002) 292–301, doi:[10.1016/S0921-5093\(01\)01528-3](https://doi.org/10.1016/S0921-5093(01)01528-3).
- [16] O. Ludwig, J.M. Drezet, P. Ménézès, C.L. Martin, M. Suéry, Rheological behavior of a commercial AA5182 aluminum alloy during solidification, *Mat. Sci. Eng. A* 413 (2005) 174–179, doi:[10.1016/j.msea.2005.09.087](https://doi.org/10.1016/j.msea.2005.09.087).
- [17] T. Koshikawa, M. Bellet, C.A. Gandin, H. Yamamura, M. Bobadilla, Experimental study and two-phase numerical modeling of macrosegregation induced by solid deformation during punch pressing of solidifying steel ingots, *Acta Mater.* 124 (2017) 513–527, doi:[10.1016/j.actamat.2016.11.023](https://doi.org/10.1016/j.actamat.2016.11.023).
- [18] K. Miyazawa, K. Schwerdtfeger, Macrosegregation in continuously cast steel slabs: preliminary theoretical investigation on the effect of steady state bulging, *Arch Eisenhüttenwes.* 52 (1981) 415–422, doi:[10.1002/srin.198104599](https://doi.org/10.1002/srin.198104599).
- [19] T. Kajatani, J.M. Drezet, M. Rappaz, Numerical simulation of deformation-induced segregation in continuous casting of steel, *Metall. Mater. Trans. A* 32 (2001) 1479–1491, doi:[10.1007/s11661-001-0236-1](https://doi.org/10.1007/s11661-001-0236-1).
- [20] M. Wu, J. Domitner, A. Ludwig, Using a two-phase columnar solidification model to study the principle of mechanical soft reduction in slab casting, *Metall. Mater. Trans. A* 43 (2012) 945–964, doi:[10.1007/s11661-011-0940-4](https://doi.org/10.1007/s11661-011-0940-4).
- [21] V.D. Fachinotti, S.L. Corre, N. Triolet, M. Bobadilla, M. Bellet, Two-phase thermo-mechanical and macrosegregation modelling of binary alloys solidification with emphasis on the secondary cooling stage of steel slab continuous casting processes, *Int. J. Numer. Eng.* 67 (2006) 1341–1384, doi:[10.1002/nme.1664](https://doi.org/10.1002/nme.1664).
- [22] C.M.G. Rodrigues, A. Ludwig, M. Wu, A. Kharicha, A. Vakhrušev, A comprehensive analysis of macrosegregation formation during twin-roll casting, *Metall. Mater. Trans. B* 50 (2019) 1334–1350, doi:[10.1007/s11663-019-01527-x](https://doi.org/10.1007/s11663-019-01527-x).
- [23] C.M.G. Rodrigues, A. Ludwig, M. Wu, A. Kharicha, A. Vakhrušev, Two-phase viscoplastic model for the simulation of twin roll casting, *J. Mater. Process. Tech.* 286 (2020) 116814, doi:[10.1016/j.jmatprotec.2020.116814](https://doi.org/10.1016/j.jmatprotec.2020.116814).
- [24] A. Vakhrušev, A. Kharicha, M. Wu, A. Ludwig, G. Nitzl, Y. Tang, G. Hackl, J. Watzinger, C.M.G. Rodrigues, Norton-Hoff model for deformation of growing solid shell of thin slab casting in funnel-shape mold, *J. Iron Steel Res. Int.* 29 (2022) 88–102, doi:[10.1007/s42243-021-00734-8](https://doi.org/10.1007/s42243-021-00734-8).
- [25] A. Olmedilla, M. Založnik, H. Combeau, DEM simulation of dendritic grain random packing: application to metal alloy solidification, *EPJ Web Conf.* 140 (2017) 1–4, doi:[10.1051/epjconf/201714006002](https://doi.org/10.1051/epjconf/201714006002).
- [26] J.P. Cordebois, T. Constantin, Viscoplastic modeling of cutting in turning, *J. Mater. Process. Tech.* 41 (1994) 187–200, doi:[10.1016/0924-0136\(94\)90060-4](https://doi.org/10.1016/0924-0136(94)90060-4).
- [27] C.J. Greenshields, OpenFOAM – the OpenFOAM foundation – user guide, version 10, CFD Direct Ltd, London, 2022 <http://foam.sourceforge.net/docs/Guides-a4/OpenFOAMUserGuide-A4.pdf>.
- [28] J. Domitner, M. Wu, A. Kharicha, A. Ludwig, B. Kaufmann, J. Reiter, T. Schaden, Modeling the effects of strand surface bulging and mechanical soft reduction on the macrosegregation formation in steel continuous casting, *Metall. Mater. Trans. A* 45 (2014) 1415–1434, doi:[10.1007/s11661-013-2060-9](https://doi.org/10.1007/s11661-013-2060-9).
- [29] R. Mehrabian, M.C. Flemings, Macrosegregation in ternary alloys, *Metall. Mater. Trans. B* 1 (1970) 455–464, doi:[10.1007/BF02811556](https://doi.org/10.1007/BF02811556).